Zhang, Haonan, Lewis, Richard J., Dugulan, A. Iulian, Li, Yang, Wang, Shuai, Wang, Zhenxing, Zeng, Jianrong, Dummer, Nicholas F. , Xi, Yanyan, Li, Yunyun, Davies, Thomas E., Wu, Mingbo, Hutchings, Graham J. and Wu, Wenting 2026. Direct oxidative carbonylation of methane to acetic acid via high-valent iron-oxo mediated water activation. Nature Communications 10.1038/s41467-026-70339-w

Publishers page: https://doi.org/10.1038/s41467-026-70339-w

ARTICLE IN PRESS

Nature Communications

https://doi.org/10.1038/s41467-026-70339-w

Article in Press

Direct oxidative carbonylation of methane to acetic acid via high-valent iron-oxo mediated water activation

Received: 22 August 2025

Accepted: 23 February 2026

[redacted]

Cite this article as: Zhang, H., Lewis, R.J., Dugulan, A.I. *et al.* Direct oxidative carbonylation of methane to acetic acid via high-valent iron-oxo mediated water activation. *Nat Commun* (2026). https://doi.org/10.1038/s41467-026-70339-w

Haonan Zhang, Richard J. Lewis, A. Iulian Dugulan, Yang Li, Shuai Wang, Zhenxing Wang, Jianrong Zeng, Nicholas F. Dummer, Yanyan Xi, Yunyun Li, Thomas E. Davies, Mingbo Wu, Graham J. Hutchings & Wenting Wu

We are providing an unedited version of this manuscript to give early access to its findings. Before final publication, the manuscript will undergo further editing. Please note there may be errors present which affect the content, and all legal disclaimers apply.

If this paper is publishing under a Transparent Peer Review model then Peer Review reports will publish with the final article.

ARTICLE IN PRESS

© The Author(s) 2026. **Open Access** This article is licensed under a Creative Commons Attribution 4.0 International License, which permits use, sharing, adaptation, distribution and reproduction in any medium or format, as long as you give appropriate credit to the original author(s) and the source, provide a link to the Creative Commons licence, and indicate if changes were made. The images or other third party material in this article are included in the article's Creative Commons licence, unless indicated otherwise in a credit line to the material. If material is not included in the article's Creative Commons licence and your intended use is not permitted by statutory regulation or exceeds the permitted use, you will need to obtain permission directly from the copyright holder. To view a copy of this licence, visit http://creativecommons.org/licenses/by/4.0/.

Direct oxidative carbonylation of methane to acetic acid via high-valent iron-oxo mediated water activation

Haonan Zhang[1]†, Richard J. Lewis[2]†, A. Iulian Dugulan[3]†, Yang Li[1], Shuai Wang[1], Zhenxing Wang[4], Jianrong Zeng[5], Nicholas F. Dummer[2], Yanyan Xi[1], Yunyun Li[1], Thomas E. Davies[2], Mingbo Wu[1,6*], Graham J. Hutchings[2*,] Wenting Wu[1*]

[1] State Key Laboratory of Heavy Oil Processing, College of Chemistry and Chemical Engineering, China University of Petroleum (East China), Qingdao 266580, P. R. China

[2] Max Planck-Cardiff Centre on the Fundamentals of Heterogeneous Catalysis FUNCAT, Cardiff Catalysis Institute, School of Chemistry, Cardiff University, Main Building, Park Place, Cardiff CF10 3AT, UK.

[3] Fundamental Aspects of Materials and Energy (FAME), Department of Radiation Science and Technology (RST), Delft University of Technology, Mekelweg 15, 2629 JB, Delft, the Netherlands.

[4] Wuhan National High Magnetic Field Center, Huazhong University of Science and Technology, Wuhan 430074, China

[5] Shanghai Synchrotron Radiation Facility, Shanghai Advanced Research Institute, Chinese Academy of Sciences, Shanghai 201204, China

[6] State Key Laboratory of Advanced Optical Polymer and Manufacturing Technology, College of Chemical Engineering, Qingdao University of Science & Technology, Qingdao 266061, P. R. China.

* Corresponding author E-mail: wuwt@upc.edu.cn (W. T. W.); hutch@cardiff.ac.uk (G.J.H.); wumb@upc.edu.cn (M. B.W.)

† Haonan Zhang, Richard J. Lewis, and A. Iulian Dugulan contributed equally to this work.

Abstract

Direct conversion of CH_4 into value-added chemicals is impeded by the inert C-H bonds and inefficient C-C coupling. We report a spatially separated Rh-O-Fe active-site architecture that decouples CH_4 and H_2O activation through a high-valent-metal mediated radical mechanism, enabling selective CH_3COOH synthesis. In-situ infrared, operando Mössbauer spectroscopy, and quasi in-situ high-field EPR reveal that O_2 oxidizes Rh and Fe to high valence states. $Rh^{(III)}$ activates CH_4 to $\bullet CH_3$, while $Fe^{(IV)}=O$ dissociates H_2O into •OH through a truncated water-gas shift pathway. •OH rapidly reacts with CO to form •COOH intermediates, which couples with $\bullet CH_3$ within the zeolite to yield CH_3COOH. This dual-site strategy circumvents kinetic limits of conventional water-gas shift and CO insertion steps. The catalyst achieves 18.2 mmol g_{cat}^{-1} h^{-1} CH_3COOH with 92% selectivity and 100-hour stability in continuous operation. This study establishes radical decoupling enabled by high-valent metal sites as a design principle for selective alkane oxidation.

Introduction

Methane (CH_4), the primary component of natural gas, stands as a critical yet underutilized carbon resource due to the formidable challenges in its selective activation and functionalization [1-3]. The direct conversion of CH_4 into C_{2+} products demand overcoming two intrinsic barriers: the high bond dissociation energy of sp^3 C-H bonds (439 kJ mol^{-1}) and the sluggish kinetics of C-C bond formation [4-6]. Acetic acid (CH_3COOH), a cornerstone chemical with an annual demand of 18 million metric tons [7,8], exemplifies this challenge, as its industrial production still relies on an indirect syngas-derived methanol carbonylation process plagued by energy intensity [9-12]. The one-step methane oxidation process for CH_3COOH production enables efficient synthesis through direct CH_4 activation under mild conditions, bypassing the complex steps required in traditional methanol carbonylation processes, such as methanol synthesis and the use of halogen promoters, thus demonstrating significant advantages in feedstock economy and process simplicity. Although this new pathway still requires further refinement, it has already provided a more atom efficient and sustainable alternative for the green production of CH_3COOH.

Current strategies for direct CH_4 oxidative still faces several critical limitations. For C-H activation, conventional strategies typically rely on unstable zero-valent metals (e.g., Rh^0) or external addition of H_2O_2 to generate •OH [13]. In some cases, the complete water-gas shift (WGS) cycle ($CO + H_2O \rightarrow CO_2 + H_2$) is involved to in-situ produce H_2O_2 [14-16], which then undergoes multiple steps to form •OH for CH_4 activation. This multistep pathway not only prolongs reaction process but with progressively declining energy efficiency, significantly limiting the overall catalytic performance. For C-C coupling with CO, a kinetically sluggish process remains the rate-determining bottleneck. For example, the methanol carbonylation proceeds efficiently through a migratory insertion of the neutral covalent ligands $•CH_3$ and *CO at a metal center, facilitated by CH_3I, enabling high-efficiency carbonylation [17]. Therefore, in the direct CH_4 carbonylation, the in-situ generated $•CH_3$ do not readily couple with neutral CO [18]. Although recent efforts have focused on enhancing •OH and $•CH_3$ concentrations or optimizing active sites [19,20], the critical C-C coupling step (involving $•CH_3$-CO vs. $•CH_3$-•COOH) in this pathway has never been experimentally verified, hindering the development of efficient catalytic systems.

To overcome the kinetic and mechanistic constraints of direct CH_4 carbonylation, we report a catalyst design that integrates C-H activation with spatially orchestrated radical coupling. By constructing Rh-O-Fe active sites within ZSM-5, the RhFe/ZSM-5 catalyst leverages a CO-assisted water activation mechanism that circumvents the inefficiencies of conventional WGS cycles. Here, $Rh^{(III)}$ can active CH_4 to generate $•CH_3$, while O_2 treatment sustains the dynamic valence transition of $Rh^{(III)}$, and simultaneously oxidizes Fe sites to form $Fe^{(IV)}$=O species, this high-valent Fe-oxo entity facilitates direct cleavage of H_2O into •OH, which rapidly react with CO to produce •COOH intermediates. These subsequently couple with Rh-derived $•CH_3$ species within the confined micropores of the zeolite to form CH_3COOH. This integrated mechanism bridges the long-standing gap between CH_4 activation and selective C-C bond coupling, providing a new paradigm for efficient and scalable natural gas valorization.

Results

Catalytic performance of CH_4 carbonylation into acetic acid

Monometallic ZSM-5-based catalysts with 0.6 wt% metal loading (Rh, Fe, Ni, Co, Cu, Zn, Ag, Pd, Au, Re, Pt, Mo) were synthesized via a template-free seeded growth method and evaluated in a batch reactor. Among these, Rh/ZSM-5 exhibited the highest catalytic performance, achieving a CH_3COOH yield of 3.2 mmol g_{cat}^{-1} h^{-1} with a selectivity of 61% at 463 K, as determined by GC and ^1H NMR (Supplementary Figure 1-2). Notably, the Fe monometallic has little reactivity. In contrast, introducing Fe into Rh/ZSM-5 to form RhFe/ZSM-5 significantly improved catalytic performance, yielding 18.2 mmol g_{cat}^{-1} h^{-1} of CH_3COOH with a selectivity of 91.8% at 463 K under optimized reaction conditions (Table 1 entry 1, Supplementary Figure 3-4). The corresponding TOF reached ~216 h^{-1}, which is ~2.5 times that of monometallic Rh/ZSM-5 (92 h^{-1}) (Supplementary Figure 5). It is worth mentioning that the reaction was initiated at 363 K (Table 1 entry 2). This performance was significantly higher than AuFe/ZSM-5, PdFe/ZSM-5, RuFe/ZSM-5, PtFe/ZSM-5, RhNi/ZSM-5, RhCu/ZSM-5, and different supports, as well as previously reported catalysts in the literature (Figure 1a, Supplementary Figure 6-7, and Supplementary Table 1).

Furthermore, when Rh/ZSM-5 and Fe/ZSM-5 catalysts were physically mixed and tested under identical reaction conditions, no significant improvement in CH_3COOH yield or selectivity was observed compared with Rh/ZSM-5 (Supplementary Figure 2b), highlighting the crucial role of the synergistic interaction between Rh and Fe in RhFe/ZSM-5. The lower activity of the spatially separated RhFe/ZSM-I catalyst further confirms that Rh-Fe synergy is essential for high performance. Highly active Rh-Fe sites not only enhance CH_4's C-H bond activation but also modify the reaction pathway of CH_4 oxidative coupling. Additionally, a systematic investigation of Fe content, while maintaining Rh loading at 0.6 wt.%, revealed a gradual increase in both CH_3COOH yield and selectivity (Supplementary Figure 8), further demonstrating that the Fe introduction plays a key role in optimizing the reaction mechanism.

For comparison, a catalyst was synthesized using a commercial ZSM-5 (Si:Al=18) support via an impregnation method (denoted as RhFe/ZSM-5-C), and exhibited a significantly lower

CH_3COOH yields of 5.08 mmol g_{cat}^{-1} h^{-1} with a selectivity of 55.5% (Supplementary Figure 9). BET surface area analysis revealed similar values for ZSM-5-C (373 m^2/g) and ZSM-5 (338 m^2/g), indicating that the differences in catalytic performance stem primarily from variations in metal active sites or acidity rather than textural properties (Supplementary Figure 10).

CH_3COOH formation was observed only when CH_4, CO, and O_2 were simultaneously present, as no detectable products were detected in control experiments omitting any of these components (Table 1, Entry 3-5). These findings demonstrate that CH_4, CO, O_2, and H_2O are all essential for CH_3COOH production. Additionally, when H_2 was used as a substitute for CO, only C_1 oxygenates, such as CH_3OH, HCOOH, were detected (Supplementary Figure 11a, Supplementary Table 2 Entry 1). This suggests that CH_3COOH is produced through the C-C coupling of CH_4 and CO, rather than from environmental contaminants or the catalyst itself. In addition, comparative experiments performed with CH_3COOH in the presence and absence of CO confirmed that CO_2 is predominantly formed through CO oxidation (Supplementary Figure 11b). Under standard methane oxidation conditions, the rate of CO_2 production reached 41.6 mmol g_{cat}^{-1} h^{-1}, surpassing that from CH_3COOH. For clarity, both liquid-phase selectivity (>92% toward CH_3COOH among oxygenated products) and total carbon selectivity (including CO_2, 42.3% for CH_3COOH) are provided (Supplementary Figure 12-13). These results indicate that, although the catalyst shows high selectivity to acetic acid in the liquid phase, the oxidation of CO to CO_2 represents a major competing pathway and warrants further optimization in future studies.

To confirm the heterogeneous nature and stability of the catalyst, further control experiments were conducted [21]. In the absence of catalyst, as well as in the presence of $FeCl_2$, $Rh(NO_3)_3$, or a mixture of these species, no catalytic activity was observed (Supplementary Table 2 Entry 2-5). Hot filtration experiments further confirmed the heterogeneous nature of the catalytic process, as no additional reaction occurred after 2 hours (Figure 1b). The stability of RhFe/ZSM-5 was evaluated over five reaction cycles, showing negligible leaching of Rh and Fe species, as determined by ICP analysis (Supplementary Table 3). In addition, batch reactions conducted under lower CH_4 partial pressure in air and CO achieved a CH_4 conversion of up to 24.8% within 3 h

(Figure 1c), with > 98% selectivity to CH_3COOH. Even when prolonging reaction time to 6 h, no methanol and formic acid were not detected by ^{1}H-NMR (Supplementary Figure 14). Furthermore, this reaction system is effective not only for CH_4 but also for ethane, which yield acids with an additional carbon atom (Supplementary Figure 15).

Identification of active sites

The synergy observed by the presence of both Rh and Fe in the CH_4 reaction to CH_3COOH over the prepared ZSM-5-based catalyst required careful study to elucidate a structure-activity relationship. XRD analysis shows that the ZSM-5 crystal structure was well preserved in Fe/ZSM-5, Rh/ZSM-5, and RhFe/ZSM-5 [22], with no characteristic diffraction peaks corresponding to Rh and Fe metals (Supplementary Figure 16). The isolated Fe and RhO_X nanoparticles species were detected in the ZSM-5 as confirmed by the annular dark-field scanning transmission electron microscopy (AC-HAADF-STEM) and EDX (Figure 2a-b, Supplementary Figure 17-18). In the UV-vis spectrum (Supplementary Figure 19), no obvious absorption at >400 nm was observed, which implies that homogeneous isolated Fe species was confined in the micropores [3,23].

X-ray absorption fine structure spectroscopy (XAS) was used to systematically study electronic structures and coordination environments of as-prepared catalysts. In the Fourier transform (FT) k^3-weighted extended EXAFS spectrum, the absence of Fe-Fe shell verifies that the Fe atoms were atomically dispersed in the Fe/ZSM-5 and RhFe/ZSM-5 (Figure 2c), Rh exhibits a RhO_X curve similar to that of Rh_2O_3 (Figure 2d). For Rh/ZSM-5, the best fitting of the Rh-O backscattering path reveals the Rh-O coordination numbers of 6 in the first coordination shell (Supplementary Figure 20, Supplementary Table 4). For Fe/ZSM-5, the major peak at ~1.50 Å in Fe K-edge EXAFS spectrum could be attributed to the Fe-O configurations with a coordination number of 4. For RhFe/ZSM-5, a primary peak at 1.52 Å could be attributed to Rh-O shell and Rh-O-Fe in second shell in 2.42 Å was observed (Figure 2d), which is longer than that of Fe-O-Fe in Fe/ZSM-5 (2.34 Å), which suggests the presence of an Rh-O-Fe structure in RhFe/ZSM-5.

To confirm the Rh-O-Fe structure, ^{57}Fe Mössbauer spectra of Fe/ZSM-5 and RhFe/ZSM-5 were collected at 4.2 K using a ^{57}Co(Rh) source (Figure 2e-f, Supplementary Table 5). The spectra were fitted with a doublet (assigned to dimeric high-spin Fe$^{(III)}$-Fe$^{(III)}$ species) and a broad sextet (assigned to isolated Fe$^{(III)}$ ions). Minor isolated Fe$^{(II)}$ species (2-3%) were also detected. The Fe$^{(III)}$ paramagnetic doublet at 4.2 K indicates well-distributed Fe species without sufficient neighboring Fe atoms to generate a magnetic field, even at cryogenic temperatures. The doublet suggests spin relaxation (spin-flipping) due to coupling between at least two neighboring Fe atoms, supporting a dimeric structure. When Fe$^{(III)}$ ions are spaced >1.5 nm apart, slow spin-spin relaxation results in paramagnetic hyperfine splitting. The broad sextets correspond to isolated Fe$^{(III)}$ ions with large hyperfine fields (>55 T), as shown in Supplementary Figure 21, with a maximum magnetic field distribution at ~56 T. Typical Fe oxide clusters (~54 T) are likely absent. Paramagnetic hyperfine splitting in Fe-ZSM-5 aligns with prior observations [24]. Isomer shifts for Fe$^{(III)}$ species suggest octahedral extra-framework coordination, as tetrahedral positions would exhibit smaller shifts (~0.4 mm/s). The Rh-Fe sample shows more dimeric species (28%) than the Fe-only sample (18%), potentially indicating Fe-Rh dimer formation, consistent with XAS results.

We further investigated the interaction between Fe and Rh through electronic structure analysis. The Rh K-edge XANES spectrum (Supplementary Figure 22a) showed that the introduction of Fe into Rh/ZSM-5 increased the oxidation state of Rh in RhFe/ZSM-5 when compared to that in Rh/ZSM-5. Similarly, Fe K-edge XANES spectrum (Supplementary Figure 22b) revealed that Fe in RhFe/ZSM-5 has a lower oxidation state than in Fe/ZSM-5, indicating electron transfer from Rh to Fe. The oxidation state of Fe is between +2 and +3, while Rh is below +3. This charge redistribution was further supported by the Rh 3*d* XPS spectrum (Supplementary Figure 23), where the characteristic peaks at 312.5 eV and 307.7 eV in Rh/ZSM-5 shift to 312.9 eV and 308.2 eV in RhFe/ZSM-5, suggesting an increased electron density on Fe in RhFe/ZSM-5.

To further elucidate the unique electronic structure of the catalyst, we carried out in-situ CO-DRIFTS measurements (Supplementary Figure 24). ZSM-5 and monometallic Fe/ZSM-5 show characteristic peaks of gaseous CO at 2171 cm^{-1} and 2118 cm^{-1}, whereas Rh/ZSM-5 exhibits linear CO adsorption bands at 2107 cm^{-1} and 2040 cm^{-1}. Notably, RhFe/ZSM-5 catalyst shows a distinct blue shift to 2104 cm^{-1} and 2037 cm^{-1}, indicating a decrease in the electron density of Rh sites. This directly reflects the electronic interaction between Rh and Fe, specifically, electron transfer from Rh to Fe, and is fully consistent with XPS and XANES data. In addition, the appearance of a bridged CO adsorption peak at 1860 cm^{-1} further confirms the presence of Rh nanoparticles, in agreement with HAADF-STEM observations.

To directly investigate the influence of acidic sites on catalytic performance, we prepared a series of RhFe/ZSM-5-X catalysts with identical metal loadings but varying SiO_2/Al_2O_3 ratios (X = 18, 25, 40, 60, 80). NH_3-TPD and pyridine adsorption infrared spectroscopy (Py-IR) results show that the acidity of the catalysts significantly decreases with increasing SiO_2/Al_2O_3 ratios (Supplementary Figure 25a-b). Catalytic performance tests (Supplementary Figure 25c) indicate that both the yield and selectivity of CH_3COOH decrease markedly as the support SiO_2/Al_2O_3 increases. Among these, RhFe/ZSM-5-18 exhibits the best CH_3COOH performance (18.2 mmol g_{cat}^{-1} h^{-1}), while RhFe/ZSM-5-80 shows a substantial decline in activity (0.4 mmol g_{cat}^{-1} h^{-1}). This clearly demonstrates that zeolite acidity is a key factor in maintaining high catalytic performance.

To further differentiate the acidic contribution, Na^+ ion exchange was performed on RhFe/ZSM-5 (SiO_2/Al_2O_3=18) to obtain RhFe/Na-ZSM-5. Py-IR reveals a significant decrease in both Brønsted and Lewis acid sites, confirming effective neutralization of the acidic sites (Supplementary Figure 26a). Correspondingly, the CH_3COOH yield over RhFe/Na-ZSM-5 decreases to 3.8 mmol g_{cat}^{-1} h^{-1}, further proving that acidic sites (particularly exchangeable H^+) are indispensable for high catalytic activity (Supplementary Figure 26b). In CO-TPD (Supplementary Figure 26c), RhFe/ZSM-5 exhibits a strong CO desorption peak at 665 K, indicating its strong adsorption capacity for CO. In contrast, the desorption peak for RhFe/Na-ZSM-5 shifts to 553 K with reduced intensity, demonstrating that Na^+ exchange not only weakens acidity but also the CO adsorption strength of catalyst.

Comparison with Conventional WGS and Key Steps

Previous studies have proposed that water in the Water-Gas Shift (WGS) reaction plays a crucial role in CH_4 activation [14,25], as H_2 generated from WGS facilitates the conversion of O_2 into

H_2O_2, which subsequently produces •OH species for CH_4 activation. However, this multi-step process introduces significant kinetic limitations that hinder overall reaction efficiency. In contrast, our RhFe/ZSM-5 catalytic system appears to follow a fundamentally different pathway.

Isotope kinetic studies in the WGS system (CO and H_2O) catalyzed by RhFe/ZSM-5 showed a kinetic isotope effect (KIE) ratio of K_H/K_D (H_2) = 4 at 463 K (Supplementary Figure 27), confirming that H_2O decomposition is the rate-determining step (RDS) in the WGS reaction. However, in the CH_4, CO, O_2, and H_2O system, the KIE ratio for CH_3COOH formation over Rh/ZSM-5 was approximately 1 (Figure 3a, Supplementary Figure 28), whereas RhFe/ZSM-5 exhibited an inverse KIE (K_H/K_D = 0.21) (Figure 3b, Supplementary Figure 29-30), suggesting that the presence of Fe promotes H_2O activation, thereby eliminating water activation as the rate-determining step in the reaction.

Although a low concentration of H_2 was detected during WGS over RhFe/ZSM-5 (Supplementary Figure 31), the significant difference between the formation rates of H_2 and liquid products suggests that H_2 does not play a major role in CH_3COOH formation. This conclusion is further corroborated by the effect of H_2 addition on product selectivity, as the introduction of H_2 resulted in only a 1.5 increase in CH_3COOH yield, whereas methanol yield increased by 3.7 (Supplementary Figure 32). In the in-situ DRIFTS measurements of CO, O_2, and H_2O reaction system (Figure 3c and 3d), two obvious signals at 950 cm^{-1} and 932 cm^{-1} were observed on Rh/ZSM-5 and RhFe/ZSM-5, which can be assigned to side-on O_2 adsorption and O-O stretching of surface peroxo species [26-28]. Moreover, a new peak at 840 cm^{-1} and a shoulder at 864 cm^{-1} were detected on Rh/ZSM-5 (Figure 3c), attributed to the O-O stretching of adsorbed and free H_2O_2 molecules, respectively [28]. Nevertheless, these two signals were absent on RhFe/ZSM-5 (Figure 3d), indicating that H_2O_2 wasn't generated on RhFe/ZSM-5.

Identification of Active Species and Oxygen Sources

In order to study the influence of •OH, excess H_2O_2 instead of O_2 was added into the system of CH_4, CO, and H_2O (Supplementary Figure 33). Both the yield and selectivity of CH_3COOH were lower than those observed in the CH_4, CO, O_2, and H_2O reaction system. Notably, although the concentration of •OH radicals in the H_2O_2 system was significantly higher than in the CO and O_2 systems (Supplementary Figure 34), the CH_3COOH yield remained relatively low, indicating that •OH radicals can participate in CH_3COOH formation, but not the primary pathway of CH_4 activation. These findings demonstrate that an alternative activation mechanism must be responsible for CH_4 conversion rather than $H_2+O_2 \rightarrow H_2O_2 \rightarrow$•OH pathway.

In the isotope-labeling experiments of CH_4, CO, $^{16}O_2$, and $H_2{}^{18}O$ (Figure 3e, Supplementary Figure 35), isotopically labeled $CH_3CO^{18}OH$ was detected, whereas only $CH_3CO^{16}OH$ was observed when CH_4, CO, $^{18}O_2$, and $H_2{}^{16}O$ were used. These results confirm that the hydroxyl oxygen in CH_3COOH originates from H_2O decomposition rather than O_2. Additionally, when using CH_4, CO, O_2 and D_2O as reactants, CH_3COOD was detected, demonstrating that the hydrogen in the hydroxyl group of CH_3COOH originates from H_2O.

Reaction Intermediates and Coupling Mechanism

To explore the intermediates after introducing Fe active sites in this reaction system, we carried out in-situ Mössbauer spectroscopy analysis [29] (Figure 4a-b and Supplementary Table 6-7) and high-frequency (240 Hz) quasi in-situ electron paramagnetic resonance (HF-EPR) spectroscopy analysis (Figure 4c) [30,31]. In the in-situ Mössbauer measurements, both the source and the samples were cooled to 4.2 K after undergoing reaction at 463 K. In this way, the data can directly be compared to data obtained at room temperature, since both source and absorbers were maintained at equal temperatures, thereby experiencing similar second-order Doppler shifts.

After an initial O_2/Ar treatment (Figure 4a-b, Treatment A), the presence of $Fe^{(IV)}=O$ species were clearly in the sub-Mössbauer-spectra of Fe/ZSM-5 and RhFe/ZSM-5 (Supplementary Table 6-7), having low isomer shift values, in the 0.14-0.21 mm/s range ($Fe^{(IV)}=O$ (I) and $Fe^{(IV)}=O$ (II), represent $O=Fe^{(IV)}-O-Fe^{(IV)}=O$, and highly dispersed $Fe^{(IV)}=O$, respectively, indicating O_2 facilitates the $Fe^{(IV)}=O$ formation [32-36]. Additionally, the presence of a doublet signal at 4.2 K indicates the spin relaxation effects in highly dispersed species-the doublet (cyan) with 0.21 mm/s isomer shift being assigned to diiron (IV) complexes, $O=Fe^{(IV)}-O-Fe^{(IV)}=O$, in the Fe/ZSM-5 [37]. Simultaneously, the observation of a well-defined sextuplet signal at 4.2 K (Figure 4a) (magenta sub-spectrum) with such highly dispersed species, indicates the presence of superexchange interactions over long-range, mediated by the oxygen atoms [38]. The superexchange interactions change the spin state at the oxoiron (IV) sites [39], as evidenced by the lower measured isomer shift values (0.14-0.16 mm/s), suggesting the presence of high-spin Fe$^{(IV)}$ species. This result is consistent with the high-field EPR (HF-EPR) spectra (15 K, 240 Hz) (Figure 4c Treatment A) after 12 h O_2 treatment at 463 K, where the disappearance of Fe and Rh signals coincided with the oxidation of Fe to Fe$^{(IV)}$ (S=2) and Rh to Rh$^{(III)}$ (S=0) (Supplementary Figure 36).

The second dimeric doublet (Figure 4a, red colour) in the Mössbauer spectra measured after the O_2/Ar treatment has an isomer shift value (0.31 mm/s), which is smaller than that measured in the fresh samples (0.53/0.50 mm/s minus 0.14 mm/s correction). This could indicate the formation of mixed dimeric complexes like HO-Fe$^{(III)}$-O-Fe$^{(IV)}$=O in Fe/ZSM-5 [39]. This component is higher in the Rh-containing sample (43 vs. 30 %), due to the partial formation of mixed Rh-O-Fe species. Also, the quadrupole splitting values are relatively different in these dimeric doublet signals (1.44 vs. 1.50 mm/s), indicating higher charge asymmetry around the Fe atoms in the Rh-containing zeolite. Under the O_2/Ar reaction conditions, the content of Fe$^{(III)}$-D in RhFe-ZSM-5 (43%) is higher than that in Fe-ZSM-5 (30%). This is due to Rh's ability to donate electrons to Fe. XPS and EXAFS analysis confirm this electron transfer process, further indicating that HO-Fe$^{(III)}$-O-Rh species constitute a significant proportion of Fe$^{(III)}$-D in Fe(Rh)-ZSM-5.

Upon CO introduction (Figure 4a and b, Treatment B), the signal of dimeric iron Fe$^{(III)}$-D decreased in the Mössbauer spectra, while the signal of dispersed iron Fe$^{(III)}$-PHS (blue) increased. This suggests that CO preferentially reacts with the bridging oxygen in HO-Fe$^{(III)}$-O-Rh(Fe) dimers rather than Fe$^{(IV)}$=O (I) and Fe$^{(III)}$-D. The selective reaction of CO with the bridging oxygen disrupts long-range superexchange interactions mediated by oxygen atoms, leading to the conversion of Fe$^{(III)}$-D into Fe$^{(III)}$-PHS. The amount of Fe$^{(IV)}$ showed little change, suggesting its low reactivity in oxidizing CO, which aligns well with the EPR results (Figure 4c, treatment B).

When CH_4 was introduced (Figure 4a and b, Treatment C), the spectral contributions of Fe$^{(IV)}$ species remained largely unchanged of RhFe/ZSM-5 in Mössbauer spectroscopy, but their hyperfine parameters of Fe$^{(IV)}$ shifted more significantly than that Fe/ZSM-5, suggesting that the neighboring Rh sites play a crucial role in C-H activation, rather than the Fe$^{(IV)}$=O species. Upon CH_4 introduction to the RhFe/ZSM system post O_2/CO treatment, the HF-EPR signal re-emerged

(Figure 4c Treatment C), demonstrating that CH_4 can be activated by high-valent metals ($Fe^{(IV)}$ or $Rh^{(III)}$). Importantly, the Mössbauer spectra revealed no significant change in $Fe^{(IV)}$ species after CH_4 exposure, confirming that the observed signal in the HF-EPR originates from the reduction of $Rh^{(III)}$ to $Rh^{(II)}$, while $Rh^{(III)}$ actively participated in CH_4 activation.

Subsequent H_2O treatments (Figure 4a and b, Treatment D) appear to reset the samples to their fresh state. However, the dimeric complex in the RhFe/ZSM-5 remained with low isomer shift values (0.32-0.34 mm/s), indicating the continued presence of mixed $Fe^{(III)}$-O-Rh species. The Rh-O_2-H_2O system (Supplementary Figure 37) also exhibited a $Rh^{(II)}$ signal, proving that both $Fe^{(IV)}$ and $Rh^{(III)}$ can activate water. Notably, the signal amplitude increased markedly upon H_2O addition, indicating that high-valent metals extract •H radicals (not protons) from H_2O, concurrently generating •OH radicals.

Furthermore, in-situ infrared spectroscopy was employed to capture the key intermediates in CH_4 activation and coupling (Supplementary Figure 38). Water vapor was introduced into the in-situ cell using an N_2 carrier gas, and a baseline was recorded after stabilization. Sequential addition of CH_4 and CO yielded no significant signals corresponding to products such as *C=O in CH_3COOH. However, upon O_2 introduction, the spectrum underwent significant changes, revealing signals for •CH_3 and *C=O at 1467 cm^{-1} and 1743 cm^{-1}, respectively [40,41]. Notably, the water consumption peak at 3670 cm^{-1}, coinciding with the results of Mössbauer and HF-EPR. EPR further detected the presence of •CH_3 radicals (Supplementary Figure 39). In the in-situ FTIR spectra under condition of O_2/H_2O and O_2/H_2O /CO over Fe/ZSM-5 (Supplementary Figure 40), the vibration of CO was observed in the range of 2011-2256 cm^{-1}, while the characteristic peaks at 1576 cm^{-1} and 1352 cm^{-1} correspond to the *COOH, indicating CO hydroxylation [42]. Compared with the $O_2/H_2O/CH_4$ system (Supplementary Figure 41), $O_2/CO/H_2O/CH_4$ system shows significantly enhanced HF-EPR signals, demonstrating that CO promotes the conversion of H_2O and CH_4 into •OH and •CH_3 radicals, facilitating •COOH formation via •OH/CO coupling and subsequent CH_3COOH synthesis.

To further confirm the C-C coupling pathway, we conducted control experiments using methanol, formaldehyde, and formic acid as potential reactants under identical conditions. However, none of these compounds resulted in the formation of CH_3COOH (Supplementary Table 2, Entries 6-8), effectively ruling out a methanol-based pathway, such as the Monsanto process. When CH_3I was used as a substitute for CH_4, an increase in the yields of both CH_3COOH and CH_3OH was observed, indicating the involvement of $\bullet CH_3$ radicals in the reaction (Supplementary Figure 42).

Complementary DFT calculations further support a radical based pathway involving $\bullet CH_3$ and $\bullet COOH$ coupling, which exhibits a significantly lower energy barrier than alternative routes. Specifically, two plausible coupling mechanisms were assessed: (i) $^*CH_3$ coupling with $^*CO$, followed by hydroxylation, and (ii) $^*CH_3$ coupling directly with $^*COOH$ formed via $^*CO$ and H_2O activation. The former pathway faces a prohibitive barrier of 1.52 eV (Figure 5a), whereas the latter proceeds with a much lower barrier of 0.48 eV, aligning well with the experimental observation of $^*COOH$ intermediates. The overall reaction mechanism is summarized in Figure 5b, Supplementary Figure 43, and Supplementary Table 8. Together, these results highlight $^*COOH$ mediated C-C coupling as the energetically and mechanistically preferred carbonylation route.

Catalyst Performance and Stability

Through mechanistic insights into CH_4 oxidation, we demonstrate that supported RhFe/ZSM-5 catalysts exhibit exceptional stability in acetate acid production during batch reactions (Supplementary Figure 44). This performance was successfully translated to continuous-flow operation using RhFe/ZSM-5 in CH_4 oxidative carbonylation (Supplementary Figure 45). In the flow reactor at 503 K (Figure 5c), the RhFe/ZSM-5 catalyst maintained stable activity for 100 hours, achieving a consistent CH_3COOH productivity of 0.71 mmol g_{cat}^{-1} h^{-1} with 83% selectivity and no observable deactivation. Meanwhile, the Rh/ZSM-5 catalyst showed significantly lower performance, yielding only 0.14 mmol g_{cat}^{-1} h^{-1} with 68% CH_3COOH selectivity (Supplementary Figure 46). Comprehensive post-reaction of batch and continuous characterization revealed preserved crystallinity and valence state by XRD and XPS (Supplementary Figure 47-48), and

STEM confirmed maintained dispersion of both noble metal nanoparticles and atomic Fe sites all structural features that directly account for the outstanding catalytic stability observed (Supplementary Figure 49-50).

Discussion

In this work, we present a spatially engineered RhFe/ZSM-5 catalyst that enables efficient oxidative carbonylation of CH_4 to CH_3COOH via a distinctive synergy between radical generation and coupling. Unlike reported systems that rely on complete WGS cycles, this catalyst leverages O_2 to convert Fe sites into $Fe^{(IV)}{=}O$ species, initiating a truncated WGS-like pathway. This process facilitates the direct activation of H_2O to generate •OH. Simultaneously, $Rh^{(III)}$ centers selectively activate CH_4 to produce $•CH_3$.

A central innovation lies in the rapid and selective coupling of these radical intermediates within the confined micropores of the ZSM-5 framework. The •OH species react swiftly with CO to form •COOH intermediates, which in turn couple with Rh-derived $•CH_3$ radicals to yield CH_3COOH. This well-coordinated cascade circumvents the kinetic limitations of traditional CO insertion routes and enables a high CH_3COOH selectivity of 92% at 463 K, with a productivity of 18.2 mmol g_{cat}^{-1} h^{-1}, 5.7 times that of Rh-only systems. Furthermore, the catalyst exhibits excellent long-term stability over 100 hours of continuous operation, underscoring its practical viability.

Overall, this work establishes a new paradigm for low-temperature CH_4 valorization by integrating spatially resolved bimetallic active sites with an unconventional, WGS-inspired water activation pathway. The mechanistic insights and design principles provided here offer a promising foundation for the development of next-generation catalytic systems for the direct transformation of CH_4 into value-added C_{2+} chemicals.

Methods

Materials and Chemicals. Ferrous chloride ($FeCl_2$, AR, 99%, Macklin), Rhodium nitrate solution ($Rh(NO_3)_3$, AR, 5% in H_2O, Macklin), and other metal chlorides (Cu, Au, Pd) (AR, 99%, Macklin) were used as metal precursors. Silica solution (SiO_2, 29%-31%, Macklin), Sodium hydroxide (NaOH, AR, Macklin), sodium aluminate ($NaAlO_2$, AR, Macklin). Methane, carbon monoxide, argon, and oxygen (99.999 vol.%, Qingdao Xin ke yuan) were used as the feedstock gases. All chemicals were used as received without any further purification. Deionized water was used throughout the research.

Catalyst preparation. RhFe/ZSM-5 was synthesized using a previously reported seeded growth template-free method with slight modifications. This process included two steps: the synthesis of ZSM-5 seeds and the synthesis of RhFe/ZSM-5.

In the first step, 15 g of colloidal silica was dissolved in 7 mL of a NaOH solution (1 M) under stirring at 373 K for 1 h. A separate solution was prepared by dissolving 0.45 g of sodium aluminate in 7 mL of a NaOH solution (1 M). The two solutions were mixed to obtain a synthetic aluminosilicate gel with a molar composition of 4 Na_2O:1 Al_2O_3:36 SiO_2:460 H_2O. The gel was stirred vigorously at 373 K for 2 h and transferred to a stainless-steel autoclave for crystallization at 453 K for 48 h. The obtained crystals were collected by filtration, washed with deionized water, and dried at 373 K to produce the ZSM-5 seeds.

In the second step, a synthetic aluminosilicate gel was prepared using the same method as in the first step. Subsequently, 1.8 mL of $Rh(NO_3)_3$ solution (5% in H_2O), containing 0.12 g of ferrous chloride ($FeCl_2$) and 0.06 g of seeds was added sequentially to the gel. After stirring for 30 min, the mixture was transferred to an autoclave for crystallization at 453 K for 48 h. The obtained crystals were collected by filtration, washed with deionized water, and dried at 353 K to obtain the as-synthesized RhFe/ZSM-5. Finally, RhFe/ZSM-5 was converted to its H-form via ion exchange with ammonium chloride (0.5 M) for 12 h, followed by calcination in air at 823 K for 6 h. The different metal loading in ZSM-5 could be tuned by varying the types of metal precursors while keeping the other conditions unchanged.

Characterizations. X-ray diffraction (XRD) was performed by the diffractometer (X'Pert PRO MPD, PANalytical, Netherlands) with Cu Kα radiation (40 kV, 100 mA, λ = 0.154 nm). The scanning electron microscope (SEM, JSM-7500F, Japan) was utilized to observe material morphology. HRTEM and EDS-mapping images were captured on the Tecni G30 instrument (FEI, USA). The morphology of the samples was further observed by aberration corrected high-angle annular dark field scanning transmission electron microscope (AC-HAADF-STEM, Themis Z, Thermo Scientific, USA). The iDPC-STEM experiments were performed at 300 kV on a FEI Themis Z microscope equipped with two aberration correctors. The content of metal elements was determined by the inductively coupled plasma atomic emission spectroscopy (ICP-AES, Agilent 730, USA). The information on the electronic state of the material surface was collected via the X-ray photoelectron spectrometer (XPS, ESCALAB 250Xi, Thermo Scientific, USA), and all binding energies were calibrated to the C1s peak of surface-contaminated carbon at 284.8 eV. Raman spectra were measured on the instrument (InVia Reflex, Renishaw, England). X-ray Absorption Spectroscopy (XAS) data for Fe and Rh K-edge were collected at the BL13SSW station of the Shanghai Synchrotron Radiation Facility (SSRF) [43], and data were obtained in fluorescence excitation mode using a Lytle detector. The X-ray Absorption Near Edge Structure (XANES) and Fourier-transformed Extended X-ray Absorption Fine Structure (EXAFS) data were analyzed using ATHENA and ARTEMIS software, respectively, and MATLAB software was employed for the analysis of wavelet transformed EXAFS data. UV-Vis diffuse reflectance spectra were obtained from the spectrometer (UV-2700, Shimadzu, Japan) furnished with an integrating sphere device. The fluorescent spectra were collected by the fluorescence spectrophotometer (RF-6000, Shimadzu, Japan). In-situ diffuse reflectance infrared Fourier transform spectroscopy (DRIFTS) measurements were measured on the instrument (VERTEX70, Bruker, Germany), the mercury cadmium telluride (MCT) detector was adopted, H_2O was bubbled into the reaction by CH_4, O_2, and CO, when the temperature was raised and stabilized to 463 K. The background correction was stabilized, CH_4, O_2, and CO replaced Ar for testing. Electron paramagnetic resonance (EPR) spectroscopy measurement was performed on the instrument (Bruker EMXplus, Germany) with 5,5-dimethyl-1-pyrroline-N-oxide (DMPO) as the radical trap. The samples were dispersed in H_2O_2 aqueous solution, dissolved CH_4 and CO to detect $\bullet CH_3$ and $\bullet OH$. The gas chromatography (Scion 456C, Tianmei, China) is equipped with a thermal conductivity detector (TCD), two flame ionization detectors (FID), a methanizer, and a headspace autosampler (DK-5001A, Beijing Zhongxing, China), which were used to quantify gaseous and CH_3OH products. High-performance liquid chromatography (HPLC, Prominence-i, LC-2030 Plus, Japan) equipped with a Refractive Index Detector (RID) was used to quantify HCOOH and CH_3COOH products. Transmission ^{57}Fe Mössbauer spectra were collected at 4.2 K with a sinusoidal velocity spectrometer using a ^{57}Co(Rh) source. Velocity calibration was carried out using an α-Fe foil at room temperature. The source and the absorbing samples were kept at the same temperature during the measurements. The Mössbauer spectra were fitted using the Mosswinn 4.0 program [44]. The experiments were performed in a state-of-the-art high-pressure Mössbauer in-situ cell -

developed at Reactor Institute Delft [45].

Oxidative coupling of methane. The methane carbonylation experiment was carried out in a 50 mL high-pressure reactor (Shi ji shen lang). The catalyst (10 mg) was uniformly dispersed in 20 mL of distilled water and sonicated for 15 minutes. The reactor was purged with argon gas to replace the air for 3-5 times. Then, methane oxygen and carbon monoxide were injected at the required pressure. The reaction was carried out in 463 K for 2 h. After the reaction, when the reactor temperature is reduced to room temperature and then cooled to below 283 K with an ice bath, the gas and liquid were collected.

Cyclic experiment. The recycle test followed the same procedure. After each run, the spent catalyst was separated using filtration, washed with a large amount of H_2O, and then dried at 353 K in the vacuum oven for the next cycle. The repeated experiments were carried out under the same experimental conditions to verify the stability of the catalyst.

•OH detection experiment. Terephthalic acid was utilized as the probe for the detection of •OH via the production of 2- hydroxyterephthalic acid. Typically, 15 mg catalyst was dispersed in 20 mL terephthalic acid solution (0.5 mM). After 2 h, a certain amount of the reactant was measured on the spectrofluorometer (RF-6000, Shimadzu, Japan) after filtering. The excitation wavelength was 315 nm, and the peak value at 425 nm was observed to semi-quantify the concentration of •OH radicals.

The detection of residual H_2O_2. After the reaction, 0.1 mol/L H_2SO_4 and 0.05 mol/L potassium titanium oxalate were added to the solution, stirred for one minute, and the absorbance was measured by UV.

Mössbauer Spectroscopy in-situ study. Transmission ^{57}Fe Mössbauer spectra were collected at 4.2 K with a sinusoidal velocity spectrometer using a ^{57}Co(Rh) source. Velocity calibration was carried out using an α-Fe foil at room temperature. The source and the absorbing samples were kept at the same temperature during the measurements. The Mössbauer spectra were fitted using the Mosswinn 4.0 program. The experiments were performed in a state-of-the-art high-pressure Mössbauer in-situ cell developed at Reactor Institute Delft [45].

DFT. The spin polarization DFT calculations were conducted using the QUICKSTEP module of the CP2K-2024.3 code [46], which utilizes a combination of Gaussian and plane-wave basis sets. For the exchange-correlation functional, the Perdew-Burke-Ernzerhof (PBE) approach was implemented. Core electrons were modeled with Goedecker-Teter-Hutter pseudopotentials, while the wave functions of valence electrons were represented using a DZVP-MOLOPT-SR-GTH basis sets. 500 Ry cutoff and 60 Ry rel_cutoff was applied, during the calculations, all the atomic positions were fully relaxed until the force is smaller than $4.5 \times 10^{\wedge-4}$. The structures were optimized using the Broyden-Fletcher-Goldfarb-Shanno (BFGS) algorithm, setting the SCF convergence criterion to $1.0 \times 10^{\wedge-6}$. To account for van der Waals (vdW) interactions, the DFT-D3(BJ) method, which includes an empirical damping term, was added to the electronic energy calculations.

The free energy G is calculated by $G = E + ZPE - TS$, where E are the DFT based energy, ZPE and TS are the correction of zero point energy and entropy, respectively. Input files and data post-processing were performed using the Multiwfn program [47,48].

Data availability

Source Data are provided with this manuscript.

References

1 Tomkins, P., Ranocchiari, M. & van Bokhoven, J. A. Direct Conversion of Methane to Methanol under Mild Conditions over Cu-Zeolites and beyond. Acc Chem Res **50**, 418-425, (2017).

2 Blankenship, A., Artsiusheuski, M., Sushkevich, V. & van Bokhoven, J. A. Recent trends, current challenges and future prospects for syngas-free methane partial oxidation. Nat. Catal. **6**, 748-762, (2023).

3 Freakley, S. J. et al. Methane Oxidation to Methanol in Water. Acc Chem Res **54**, 2614-2623, (2021).

4 Qi, G. et al. Au-ZSM-5 catalyses the selective oxidation of CH_4 to CH_3OH and CH_3COOH using O_2. Nat. Catal. **5**, 45-54, (2022).

5 An, B. et al. Sulfone-decorated conjugated organic polymers activate oxygen for photocatalytic methane conversion. Angew. Chem. Int. Ed. **134**, e202204661, (2022).

6 Xing, Y. et al. Fe/Fe_3C Boosts H_2O_2 Utilization for Methane Conversion Overwhelming O_2 Generation. Angew. Chem. Int. Ed. **60**, 8889-8895, (2021).

7 Yoneda, N., Kusano, S., Yasui, M., Pujado, P. & Wilcher, S. Recent advances in processes and catalysts for the production of acetic acid. Applied Catalysis A: General **221**, 253-265, (2001).

8 Ezhova, N. N., Kolesnichenko, N. V. & Maximov, A. L. Modern Methods for Producing Acetic Acid from Methane: New Trends (A Review). Petroleum Chemistry **62**, 40-61, (2022).

9 Zhang, H. et al. A Novel Tandem Reaction System for High-Concentration Acetic Acid Production from Methane and Oxygen. Angew. Chem. Int. Ed. **64**, e202502822, (2025).

10 Zhang, H. et al. High-Valent Nickel-Induced Oxidative Coupling of Hydrogen Sulfide-Containing Methane to Acetic Acid. ACS Catal. **15**, 10897-10907, (2025).

11 Feng, S. et al. Constructing Efficient Single Rh Sites on Activated Carbon via Surface Carbonyl Groups for Methanol Carbonylation. ACS Catal. **11**, 682-690, (2021).

12 Kalck, P., Le Berre, C. & Serp, P. Recent advances in the methanol carbonylation reaction into acetic acid. Coordination Chemistry Reviews **402**, 213078, (2020).

13 Chen, W. et al. Oxidative carbonylation of methane to acetic acid on an Fe-modified ZSM-5 zeolite. Appl. Catal., B **329**, 122549, (2023).

14 Gu, F. et al. Selective catalytic oxidation of methane to methanol in aqueous medium over copper cations promoted by atomically dispersed rhodium on TiO_2. Angew. Chem. Int. Ed. **61**, e202201540, (2022).

15 Shan, J., Li, M., Allard, L. F., Lee, S. & Flytzani-Stephanopoulos, M. Mild oxidation of methane to methanol or acetic acid on supported isolated rhodium catalysts. Nature **551**, 605-608, (2017).

16 Bo, W. et al. Highly Selective Synthesis of Acetic Acid from Hydroxyl-Mediated Oxidation of Methane at Low Temperatures. Angew. Chem. Int. Ed. **64**, e202412995, (2025).

17 Howard, M. J., Jones, M. D., Roberts, M. S. & Taylor, S. A. C1 to acetyls: catalysis and process. Catal. Today **18**, 325-354, (1993).

18 Wang, W. et al. Selective Oxidation of Methane to Methanol over Au/H-MOR. J. Am. Chem. Soc. **145**, 12928-12934, (2023).

19 Zhou, Q. et al. Selective photocatalytic oxidation of methane to methanol by constructing a rapid O_2 conversion pathway over Au-Pd/ZnO. ACS Catal. **14**, 955-964, (2024).

20 Agarwal, N. et al. Aqueous Au-Pd colloids catalyze selective CH_4 oxidation to CH_3OH with O_2 under mild conditions. Science **358**, 223-227, (2017).

21 Lewis, R. J. et al. Highly efficient catalytic production of oximes from ketones using in situ generated H_2O_2. Science **376**, 615-620, (2022).

22 Zeng, M. et al. ZSM-5-confined Cr_1-O_4 active sites boost methane direct oxidation to C_1 oxygenates under mild conditions. EES Catalysis **1**, 153-161, (2023).

23 Cheng, Q. et al. Maximizing Active Fe Species in ZSM-5 Zeolite Using Organic-Template-Free Synthesis for Efficient Selective Methane Oxidation. J. Am. Chem. Soc. **145**, 5888-5898, (2023).

24 Taboada, J., Overweg, A., Kooyman, P., Arends, I. & Mul, G. Following the evolution of iron from framework to extra-framework positions in isomorphously substituted [Fe, Al] MFI with Fe mössbauer spectroscopy. J. Catal. **231**, 56-66, (2005).

25 Cheng, Q. et al. Atomically Dispersed Iron-Copper Dual-Metal Sites Synergistically Boost Carbonylation of Methane. Angew. Chem. Int. Ed. **63**, e202411048, (2024).

26 Jiang, Y. et al. Enabling Specific Photocatalytic Methane Oxidation by Controlling Free Radical Type. J. Am. Chem. Soc. **145**, 2698-2707, (2023).

27 Ryuhei Nakamura, Y. N. Primary Intermediates of Oxygen Photoevolution Reaction on TiO_2 (Rutile) Particles, Revealed by in situ FTIR Absorption and Photoluminescence Measurements. J. Am. Chem. Soc. **126**, 1290-1298, (2004).

28 Feng, N. et al. Efficient and selective photocatalytic CH_4 conversion to CH_3OH with O_2 by controlling overoxidation on TiO_2. Nat. Commun. **12**, 4652, (2021).

29 Xue, G., De Hont, R., Münck, E. & Que, L. Million-fold activation of the $[Fe_2(\mu\text{-}O)_2]$ diamond core for C-H bond cleavage. Nat. Chem. **2**, 400-405, (2010).

30 Telser, J., Krzystek, J. & Ozarowski, A. High-frequency and high-field electron paramagnetic resonance (HFEPR): a new spectroscopic tool for bioinorganic chemistry. JBIC, J. Biol. Inorg. Chem. **19**, 297-318, (2014).

31 Krzystek, J., Ozarowski, A., Telser, J. & Crans, D. C. High-frequency and -field electron paramagnetic resonance of vanadium (IV, III, and II) complexes. Coord. Chem. Rev. **301-302**, 123-133, (2015).

32 Lim, M. H. et al. An Fe^{IV}=O complex of a tetradentate tripodal nonheme ligand. Proc. Natl. Acad. Sci. U. S. A. **100**, 3665-3670, (2003).

33 Liu, K. E. et al. Kinetic and spectroscopic characterization of intermediates and component interactions in reactions of methane monooxygenase from Methylococcus capsulatus (Bath). J. Am. Chem. Soc. **117**, 10174-10185, (1995).

34 Shu, L. et al. An $Fe_2^{IV}O_2$ Diamond Core Structure for the Key Intermediate Q of Methane Monooxygenase. Science **275**, 515-518, (1997).

35 Siegbahn, P. E. M. Theoretical Model Studies of the Iron Dimer Complex of MMO and RNR. Inorg. Chem. **38**, 2880-2889, (1999).

36 Friesner, B. F. G. D. D. A. W. J. L. A. Activation of the C−H Bond of Methane by Intermediate Q of Methane Monooxygenase: A Theoretical Study. J. Am. Chem. Soc. **123**, 3836-3837, (2001).

37 Han, W.-G. & Noodleman, L. Structural model studies for the high-valent intermediate Q of methane monooxygenase from broken-symmetry density functional calculations. Inorg. Chim. Acta **361**, 973-986, (2008).

38 De Hont, R. F. et al. Mössbauer, electron paramagnetic resonance, and density functional theory studies of synthetic S = 1/2 Fe^{III}-O-Fe^{IV}=O complexes. Superexchange-mediated spin transition at the Fe^{IV}=O Site. Inorg. Chem. **49**, 8310-8322, (2010).

39 Stoian, S. A., Xue, G., Bominaar, E. L., Que, L., Jr. & Münck, E. Spectroscopic and theoretical investigation of a complex with an [O=Fe^{IV}-O-Fe^{IV}=O] core related to methane monooxygenase intermediate Q. J. Am. Chem. Soc. **136**, 1545-1558, (2014).

40 Wu, B. et al. Fe binuclear sites convert methane to acetic acid with ultrahigh selectivity. Chem **8**, 1658-1672, (2022).

41 Luo, L. et al. Water enables mild oxidation of methane to methanol on gold single-atom catalysts. Nat. Commun. **12**, 1218, (2021).

42 Liang, J. X. et al. Dual metal active sites in an Ir_1/FeO_x single-atom catalyst: a redox mechanism for the water-gas shift reaction. Angew. Chem. Int. Ed. **59**, 12868-12875, (2020).

43 Renzhong Tai, Zhentang Zhao, Overview of SSRF phase-II beamlines. Nucl. Sci. Tech. 35, 137, (2024).

44 Klencsár, Z. Mössbauer spectrum analysis by Evolution Algorithm. Nuclear Instruments and Methods in Physics Research Section B: Beam Interactions with Materials and Atoms **129**, 527-533, (1997).

45 Wezendonk, T. A. et al. Elucidating the Nature of Fe Species during Pyrolysis of the Fe-BTC MOF into Highly Active and Stable Fischer-Tropsch Catalysts. ACS Catal. **6**, 3236-3247, (2016).

46 Kühne, T. D. et al. CP2K: An electronic structure and molecular dynamics software package - Quickstep: Efficient and accurate electronic structure calculations. J chem phys **152**, 194103, (2020).

47 Tian Lu, F. C. Multiwfn: A multifunctional wavefunction analyzer. J comput chem **33**, 580-592, (2011).

48 Lu, T. A comprehensive electron wavefunction analysis toolbox for chemists, Multiwfn. J Chem Phys **161**, 082503, (2024).

Acknowledgments

This work was supported by National Natural Science Foundation of China (22322815, 22561142234, 22179146, and 22138013) (W.W), Shandong Provincial Natural Science Foundation (Grant No. ZR2025QA14), the Fundamental Research Funds for Central Universities (18CX07009A), Independent Innovation Research Project (Science and Engineering)

(20CX06072A). We thank the BL13SSW beamline (31124.02.SSRF.BL13SSW) at the Shanghai Synchrotron Radiation Facility for the XAFS.

Author Contributions Statement

W.W. conceived and supervised the project. G.J.H. and M.W. co- supervised the project. H.Z., R.J.L. and A.I.D. conducted most experiments including synthesis, characterization and testing, as well as data analysis. Y.L. (Yang Li) carried out DFT calculations section. S.W. performed characterization and testing analysis. Z.W. conducted spectrum analysis. J.Z. contributed to data analysis of the XAS spectra. N.F.D supervised the project. Y.X. conducted DRIFTS analysis. Y.L. (Yunyun Li) conducted an analysis of the mass spectrometry. T.E.D. provided advice and expertise. H.Z., W.W., and G.J.H. wrote and revised the paper. All authors discussed the paper.

Competing interests Statement

The authors declare no competing interests.

Table 1. Catalytic performance of RhFe/ZSM-5 catalysts for the oxidation of CH_4

$$CH_4+O_2+CO \longrightarrow CH_3COOH$$

Entry	Catalyst	T (K)	Reactants (MPa)			Productivity (mmol g_{cat}^{-1} h^{-1})			CH_3COOH Selectivity (%) [d]
			CH_4	O_2	CO	CH_3OH	HCOOH	CH_3COOH	
1	RhFe/ZSM-5	463	3	0.3	0.6	0.15	1.36	18.27	92
2	RhFe/ZSM-5	363	3	0.3	0.6	0.02	0.03	0.17	77
3	RhFe/ZSM-5	463	0	0.3	0.6	n.d. [c]	n.d. [c]	n.d. [c]	n.d. [c]
4	RhFe/ZSM-5	463	3	0	0.6	n.d. [c]	n.d. [c]	n.d. [c]	n.d. [c]
5	RhFe/ZSM-5	463	3	0.3	0	n.d. [c]	n.d. [c]	n.d. [c]	n.d. [c]

6	H-ZSM-5	463	3	0.3	0.6	n.d. [c]	n.d. [c]	n.d. [c]	n.d. [c]
7	Rh/ZSM-5	463	3	0.3	0.6	0.68	1.34	3.2	61
8	Fe/ZSM-5	463	3	0.3	0.6	n.d. [c]	n.d. [c]	n.d. [c]	n.d. [c]
9[a]	Rh/ZSM-5//Fe/ZSM-5	463	3	0.3	0.6	0.71	1.42	3.64	63
10 [b]	Rh/ZSM-5-C	463	3	0.3	0.6	0.4	1.15	1.89	55
11 [b]	Fe/ZSM-5-C	463	3	0.3	0.6	n.d. [c]	n.d. [c]	n.d. [c]	n.d. [c]
12 [b]	RhFe/ZSM-5-C	463	3	0.3	0.6	3.8	1.58	5.08	49

Reaction conditions: catalyst (10 mg), water (20 mL), time (2 h), stirring speed 800 rotations per minute (rpm). For entries 3-5 is the total pressure was maintained with N_2 or Ar. [a] Rh/ZSM-5 and Fe/ZSM-5 were physically mixed. [b] ZSM-5-C was obtained from Nankai University Catalyst Co Ltd, which has the same metal loading capacity and SiO_2: Al_2O_3 ratio (18) as RhFe/ZSM-5. [c] n.d., not detected. [d] CH_3COOH selectivity in liquid products.

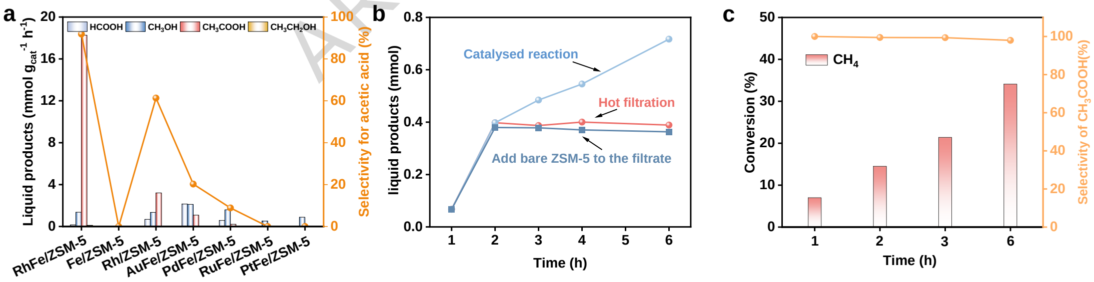

Figure 1. Catalytic performance evaluation of CH_4 oxidative coupling reaction. (**a**) Catalytic performance with different metal over ZSM-5, reaction conditions: 463 K, 10 mg catalyst, 2 h, 20 mL H_2O, 30 bar CH_4, 3 bar O_2, 6 bar CO, and stirring speed 800 rotations per minute (rpm). (**b**) Time-dependent conversion and hot filtration test of the reaction. (**c**) Oxygenate yield and selectivity as a function of CH_4 conversion at lower CH_4 partial pressure, reaction conditions: 463 K, 10 mg catalyst, 20 mL H_2O, 121 umol CH_4, 11 bar Air, 6 bar CO, 18 bar N_2, and stirring speed

800 rotations per minute (rpm).

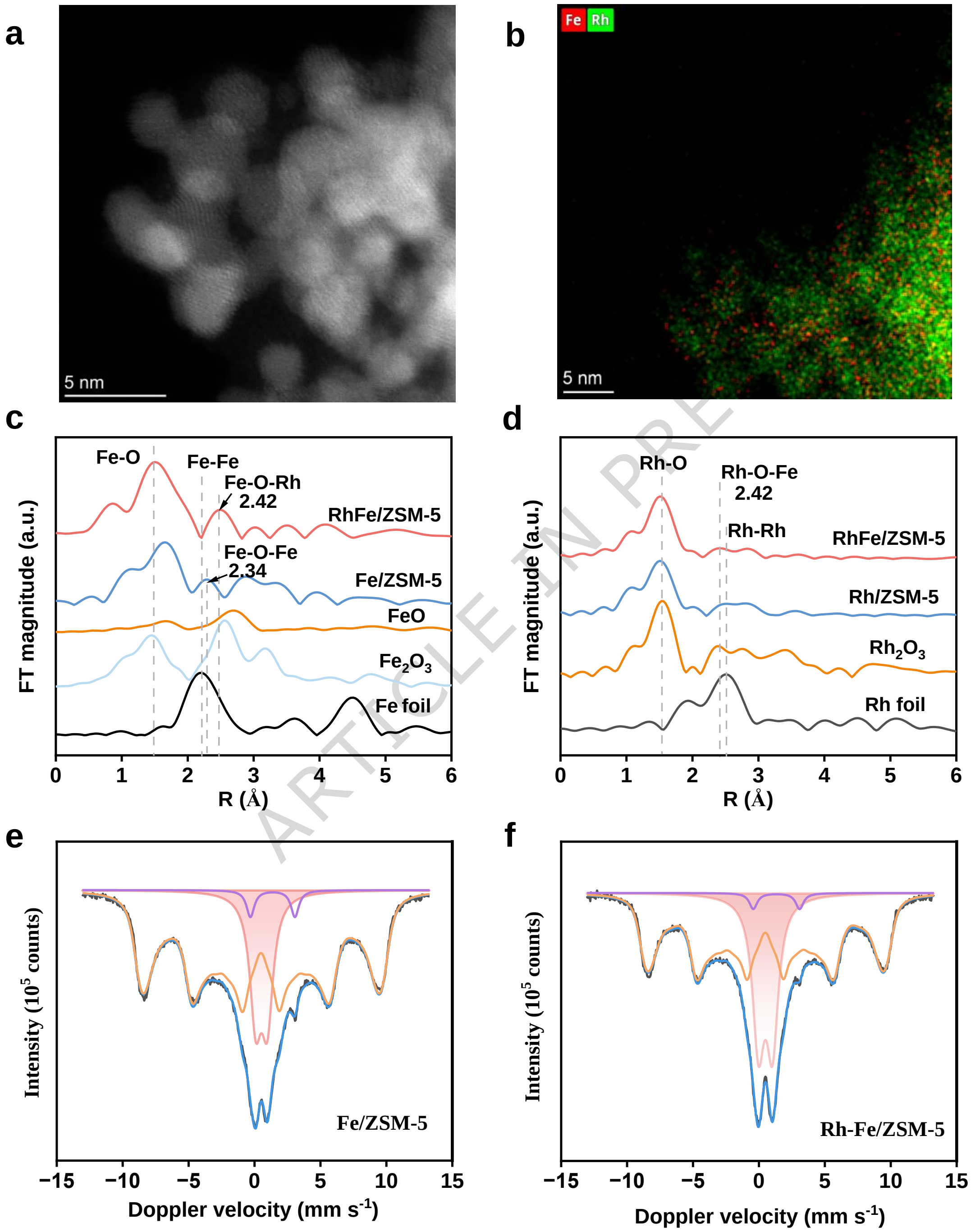

Figure 2. Structural characterization. (**a**) AC-HAADF-STEM image of RhFe/ZSM-5. (**b**) HAADF-STEM-EDS mapping of the RhFe/ZSM-5. (**c**) Fourier transform (FT) k^3-weighted EXAFS spectra of the Fe/ZSM-5, RhFe/ZSM-5, FeO, Fe_2O_3, and Fe foil. (**d**) Fourier transform

(FT) k^3-weighted EXAFS spectra of the Rh/ZSM-5, RhFe/ZSM-5, Rh_2O_3 and Rh foil. (**e-f**) ^{57}Fe Mössbauer spectra for the Fe/ZSM-5 and RhFe/ZSM-5 catalysts.

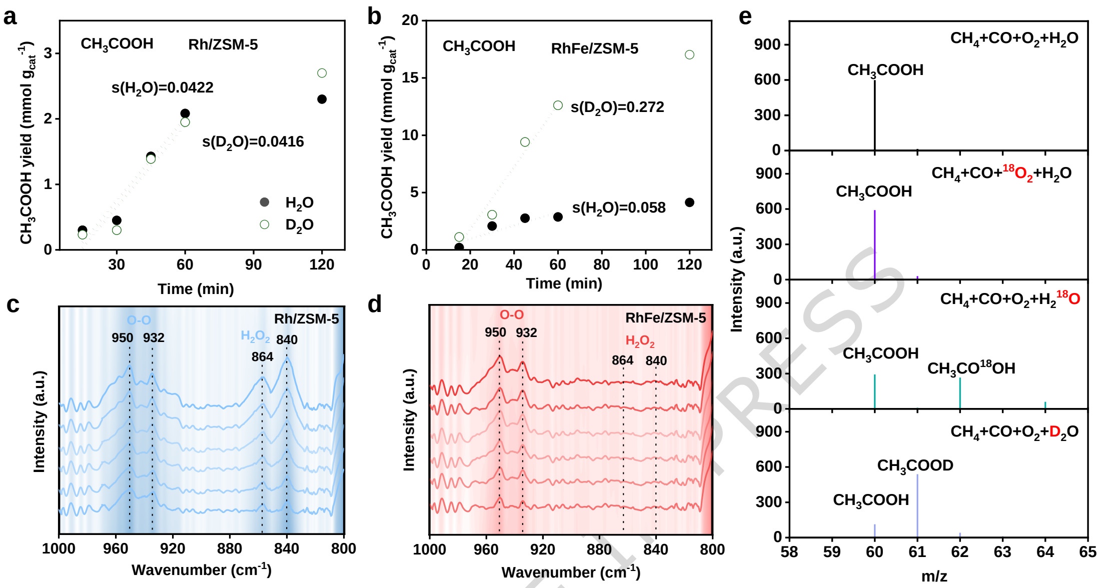

Figure 3. CH_4 adsorption and activation mechanism. (a) CH_3COOH production under H_2O and D_2O with different reaction time over Rh/ZSM-5. (**b**) CH_3COOH production under H_2O and D_2O with different reaction time over RhFe/ZSM-5. (**c-d**) Detection of H_2O_2 using in-situ DRIFTS spectra of Rh/ZSM-5 and RhFe/ZSM-5 catalysts in the presence of O_2, CO and H_2O at 463 K. (**e**) GC-MS spectra of the isotope CH_3COOH produced from CH_4 conversion when using $CH_4+CO+^{16}O_2+H_2{}^{18}O$, $CH_4+CO+^{18}O_2+H_2{}^{16}O$ and $CH_4+CO+O_2+D_2O$ as the reactants.

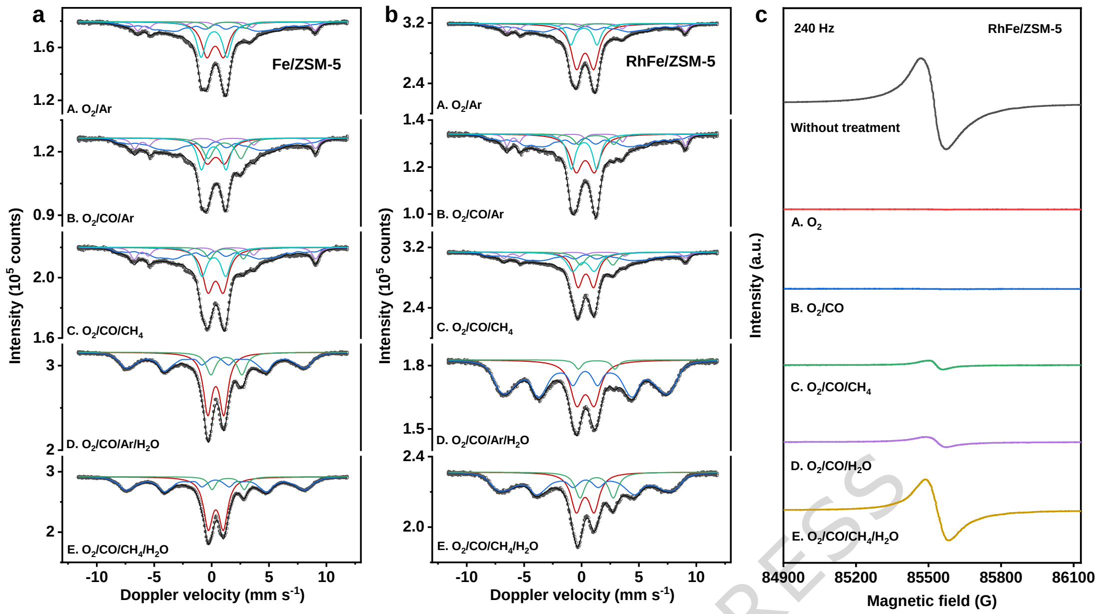

Figure 4. In-situ Mössbauer spectroscopy. (**a**) Fe/ZSM-5. (**b**) RhFe/ZSM-5. Transmission ^{57}Fe Mössbauer spectra were collected at 4.2 K with a sinusoidal velocity spectrometer using a ^{57}Co(Rh) source. Velocity calibration was carried out using an α-Fe foil at room temperature. The source and the absorbing samples were kept at the same temperature during the measurements. (**c**) In-situ High-field EPR of the catalyst during reaction. Reaction conditions: 463 K, 12 h, test conditions: 15 K, microwave frequency: 240 Hz.

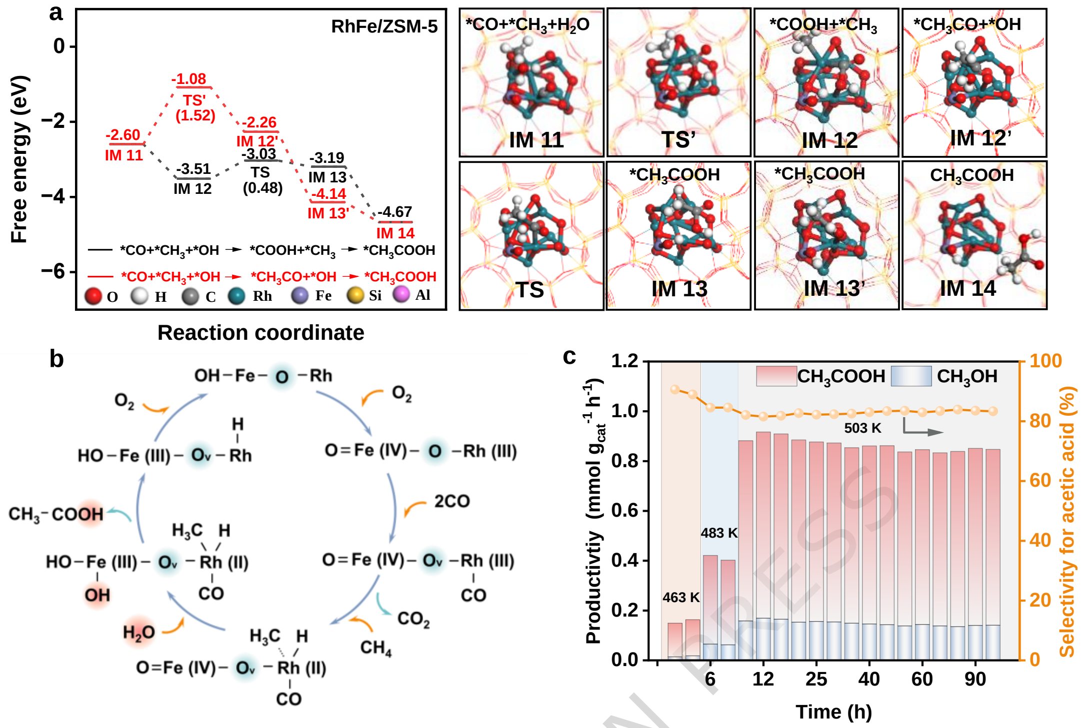

Figure 5. DFT calculations and stability in a continuous flow reactor. (a) DFT calculations of *COOH and *CH_3CO path. (b) Proposed RhFe/ZSM-5 catalytic cycle. (c) The CH_4 oxidative coupling reaction was catalyzed in a continuous regime. Reaction conditions: Before the reaction, 0.2 g of RhFe/ZSM-5 catalyst (20-40 mesh) was thoroughly mixed with 0.6 g of acid-washed quartz sand (20-40 mesh) to minimize temperature gradients, and the mixture was loaded into a stainless-steel fixed-bed reactor. 503 K, H_2O 0.3 mL/min, CH_4 20 mL/min, CO 10 mL/min, O_2 5 mL/min.

Editorial summary:

Converting methane into valuable chemicals is challenging due to its stable bonds and inefficient C–C coupling. Herein, a dual-site catalyst with high-valent metals to selectively converts methane to acetic acid with high efficiency and stability.

Peer Review Information: *Nature Communications* thanks Vitaly ORDOMSKY and the other, anonymous, reviewer(s) for their contribution to the peer review of this work. A peer review file is available.